The Astronomical Journal, 133:1658–1672, 2007 April

THE ACS SURVEY OF GALACTIC GLOBULAR CLUSTERS. I. OVERVIEW AND CLUSTERS WITHOUT PREVIOUS *HUBBLE SPACE TELESCOPE* PHOTOMETRY[1]

Ata Sarajedini
Department of Astronomy, University of Florida, Gainesville, FL 32611, USA; ata@astro.ufl.edu

Luigi R. Bedin
European Southern Observatory, Garching D-85748, Germany; lbedin@eso.org

Brian Chaboyer and Aaron Dotter
Department of Physics and Astronomy, Dartmouth College, Hanover, NH 03755, USA;
chaboyer@heather.dartmouth.edu, aaron.l.dotter@dartmouth.edu

Michael Siegel
University of Texas, McDonald Observatory, Austin, TX 78712, USA; siegel@astro.as.utexas.edu

Jay Anderson
Department of Physics and Astronomy, Rice University, Houston, TX 77005, USA; jay@eeyore.rice.edu

Antonio Aparicio
University of La Laguna, and Instituto de Astrofísica de Canarias, E-38200 La Laguna, Canary Islands, Spain; antapaj@iac.es

Ivan King
Department of Astronomy, University of Washington, Seattle, WA 98195-1580, USA; king@astro.washington.edu

Steven Majewski
Department of Astronomy, University of Virginia, Charlottesville, VA 22904-4325, USA; srm4n@virginia.edu

A. Marín-Franch
Department of Astronomy, University of Florida, Gainesville, FL 32611, USA; amarin@astro.ufl.edu

Giampaolo Piotto
Dipartimento di Astronomia, Università di Padova, 35122 Padova, Italy; piotto@pd.astro.it

I. Neill Reid
Space Telescope Science Institute, Baltimore, MD 21218, USA; inr@stsci.edu

and

Alfred Rosenberg
Instituto de Astrofísica de Canarias, E-38200 La Laguna, Canary Islands, Spain; alf@iac.es
Received 2006 October 2; accepted 2006 December 14

ABSTRACT

We present the first results of a large Advanced Camera for Surveys (ACS) survey of Galactic globular clusters. This *Hubble Space Telescope* (*HST*) Treasury project is designed to obtain photometry with S/N (signal-to-noise ratio) $\gtrsim$10 for main-sequence stars with masses $\gtrsim$0.2 $M_{\odot}$ in a sample of globulars using the ACS Wide Field Channel. Here we focus on clusters without previous *HST* imaging data. These include NGC 5466, NGC 6779, NGC 5053, NGC 6144, Palomar 2, E3, Lyngå 7, Palomar 1, and NGC 6366. Our color-magnitude diagrams (CMDs) extend reliably from the horizontal branch to as much as 7 mag fainter than the main-sequence turnoff and represent the deepest CMDs published to date for these clusters. Using fiducial sequences for three standard clusters (M92, NGC 6752, and 47 Tuc) with well-known metallicities and distances, we perform main-sequence fitting on the target clusters in order to obtain estimates of their distances and reddenings. These comparisons, along with fitting the cluster main sequences to theoretical isochrones, yield ages for the target clusters. We find that the majority of the clusters have ages that are consistent with the standard clusters at their metallicities. The exceptions are E3, which appears $\sim$2 Gyr younger than 47 Tuc, and Pal 1, which could be as much as 8 Gyr younger than 47 Tuc.

Key words: globular clusters: individual (E3, Lyngå 7, NGC 5053, NGC 5466, NGC 6144, NGC 6366, NGC 6779, Palomar 1, Palomar 2) — Hertzsprung-Russell diagram

1. INTRODUCTION

We present the first results of a 132 orbit *Hubble Space Telescope* (*HST*) Treasury program to conduct an Advanced Camera for Surveys (ACS) survey of Galactic globular clusters (GCs). This project is designed to obtain uniform photometry with S/N (signal-to-noise ratio) $\gtrsim$10 for stars as faint as 0.2 $\mathcal{M}_{\odot}$ ($M_V \lesssim$ 10.7) along the main sequence for approximately half of the nearest known Milky Way GCs, using the Wide Field Channel (WFC) of the ACS. The survey will produce an image atlas and source catalog with astrometry and photometry for stars in the target clusters, using both newly obtained ACS observations and archival ACS and Wide Field Planetary Camera 2 (WFPC2)

[1] Based on observations with the NASA/ESA *Hubble Space Telescope*, obtained at the Space Telescope Science Institute, which is operated by AURA, Inc., under NASA contract NAS5-26555, under program GO-10775 (PI: A. Sarajedini).

TABLE 1
OBSERVING LOG

Cluster	R.A. (J2000.0)	Decl. (J2000.0)	l (deg)	b (deg)	Data Set	UT Date	Filter	Exp. Time (s)
NGC 5466	14 05 27.3	+28 32 04	42.15	73.59	J9L903	2006 Apr 12	F606W	$1 \times 30, 5 \times 340$
							F814W	$1 \times 30, 5 \times 350$
NGC 6779 (M56)	19 16 35.5	+30 11 05	62.66	8.34	J9L905	2006 May 11	F606W	$1 \times 20, 5 \times 340$
							F814W	$1 \times 20, 5 \times 350$
NGC 5053	13 16 27.0	+17 41 53	335.69	78.94	J9L902	2006 Mar 6	F606W	$1 \times 30, 5 \times 340$
							F814W	$1 \times 30, 5 \times 350$
NGC 6144	16 27 14.1	−26 01 29	351.93	15.70	J9L943	2006 Apr 15	F606W	$1 \times 25, 5 \times 340$
							F814W	$1 \times 25, 5 \times 350$
Palomar 2	04 46 05.9	+31 22 51	170.53	−9.07	J9L908	2006 Aug 8	F606W	5×380
							F814W	5×380
E3	09 20 59.3	−77 16 57	292.27	−19.02	J9L906	2006 Apr 15	F606W	$1 \times 5, 4 \times 100$
							F814W	$1 \times 5, 4 \times 100$
Lyngå 7	16 11 03.0	−55 18 52	328.77	−2.79	J9L904	2006 Apr 7	F606W	$1 \times 35, 5 \times 360$
							F814W	$1 \times 35, 5 \times 360$
Palomar 1	03 33 23.0	+79 34 50	130.07	19.03	J9L901	2006 Mar 17	F606W	$1 \times 15, 5 \times 390$
							F814W	$1 \times 15, 5 \times 390$
NGC 6366	17 27 44.3	−05 04 36	18.41	16.04	J9L907	2006 Mar 30	F606W	$1 \times 10, 4 \times 140$
							F814W	$1 \times 10, 4 \times 140$

NOTE.—Units of right ascension are hours, minutes, and seconds, and units of declination are degrees, arcminutes, and arcseconds.

imaging, when available. In the spirit of the *HST* Treasury concept, the overall goal of this "legacy" survey is to investigate fundamental aspects of Galactic GCs (e.g., luminosity functions, reddenings, distances, ages, proper motions, and binary fractions) and provide a lasting contribution to cluster studies by creating a uniquely deep and uniform database of a large sample of Galactic GCs.

Our target list includes 65 GCs chosen by a number of criteria, the most important of which are proximity to the Sun $[(m - M)_0 \leq 16.5]$ and low reddening $[E(B - V) \leq 0.35]$. However, we have also included a few clusters of intrinsic interest, such as those believed to be associated with the Sagittarius dwarf spheroidal galaxy and a number of clusters in the direction of the Galactic bulge. The full details of our target list will be published in a forthcoming paper.

This first paper in our survey is concerned with GCs in our target list that have not been previously imaged by *HST*. These include the metal-poor clusters NGC 5466, NGC 6779 (M56), NGC 5053, and NGC 6144; the intermediate-metallicity cluster Palomar 2; and the metal-rich clusters E3, Lyngå 7, Palomar 1, and NGC 6366. The clusters are ordered, here as elsewhere in this paper, by metallicity. In § 2 we summarize the observations and data reduction, which are generally similar for all clusters in our program. The resultant color-magnitude diagrams (CMDs) are presented and discussed in § 3. Main-sequence fits and comparisons with theoretical isochrones are included in §§ 4 and 5, respectively. Section 6 presents a summary of our results.

2. OBSERVATIONS AND DATA REDUCTION

The observations of our program clusters were obtained with the *HST* ACS WFC instrument in the F606W ($\sim V$) and F814W ($\sim I$) filters. Each cluster was centered in the ACS field and observed for two orbits, one orbit for each filter, with one short exposure per filter (except for Pal 2) and four to five long-exposure frames. The long exposures were dithered to fill in the gap between the two CCDs of the ACS. Table 1 presents the log of the observations.

The process of deriving photometry from the short and long exposures and combining the results will be fully described in a forthcoming paper (J. Anderson et al. 2007, in preparation). To summarize, we reduced each _FLT exposure independently, using the program img2xym_WFC.09x10, which is documented in Anderson & King (2006). The program uses an array of 9×10 point-spread functions (PSFs) to treat the spatial variability of the WFC PSF. The routine also allows for a spatially constant perturbation adjustment for the PSF to better match each individual exposure. (The perturbation adjustment for the PSF was possible only on exposures that had a sufficient number of well-exposed stars; this ruled out all of the short exposures.)

The above computer program went through each image pixel by pixel and used the PSF model to get a flux and a position for every source that had no brighter neighbors within 3 pixels and had at least 50 e^- above sky in a 3×3 pixel aperture. We correct the source's position for distortion using the prescription in Anderson (2006) and find the transformation from each frame into a single reference frame centered on the cluster core.

We then collate the deep star lists in the reference frame, identifying a star wherever there are three or more coincident detections in the deep exposures for each filter. This collation procedure naturally removes any cosmic rays or warm pixels that may have strayed into the deep lists for the individual exposures. We now have one star list for each of the two filters. This list contains only stars that are below the saturation limit in the deep exposures. Since each star in this list has been observed in a minimum of three exposures independently, we also have an estimate of the error in its photometry from the rms magnitude about the mean of the independent observations.

We supplement this list with the star lists for the short exposures. We first find an empirical photometric zero-point offset between the short and deep exposures and add to the deep list for each filter any star in the short exposures that is within 0.75 mag of saturation or brighter in the deep list. Stars that are saturated in the short exposures are measured by fitting the PSF to their unsaturated pixels and are included in the list, although their photometry and astrometry are less accurate. Thus, in the end, we have a list of stars found in each of the two filters. Our final star catalog is produced by merging the F606W and F814W lists, keeping only stars found in both filters. It is important to

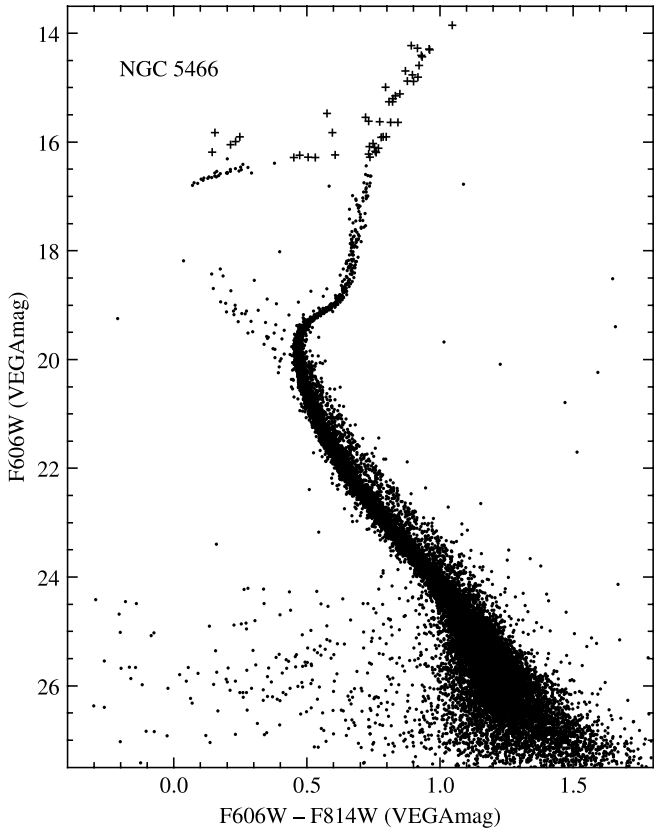

FIG. 1.—CMD for NGC 5466 in the VEGAmag system. The plus signs represent stars that are affected by at least one saturated pixel in either or both of the F606W and F814W images. This diagram contains 21,449 stars and extends to approximately 12% of the tidal radius of 34′ (Harris 1996).

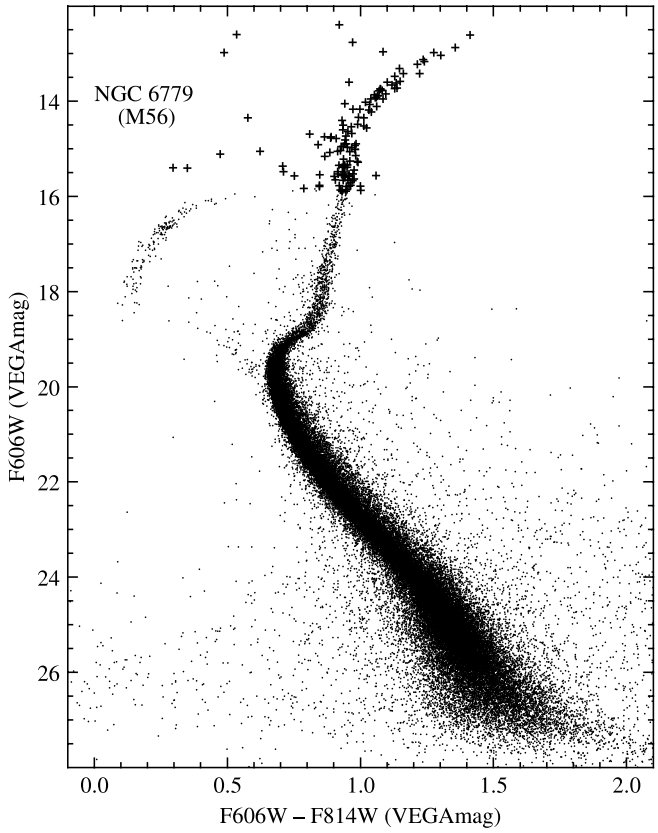

FIG. 2.—Same as Fig. 1, except that the CMD of NGC 6779 (M56) is shown, containing 61,056 stars and extending to about 50% of the tidal radius of 8.5′ (Harris 1996).

emphasize at this point that this "first pass" photometry includes only the uncrowded stars (i.e., those with no brighter neighbors within 3 pixels). The "final pass" reduction, in which we relax this crowding restriction, will include many more stars and will therefore be more complete. The photometric catalog that the Treasury project makes available to the community will include only the final pass data.

The resultant instrumental magnitudes must be corrected for the effects of charge transfer efficiency (CTE) before being transformed to a standard system. To facilitate this, we rely on the formalism of Reiss & Mack (2004, hereafter RM04). We begin by noting that all of our long-exposure observations, except for those of E3, exhibit background sky values greater than $\sim 30\ e^-$. Equation (2) of RM04 suggests that, at these sky levels, the CTE correction is less than ~ 0.005 mag for all stellar magnitudes and y-coordinates. Even in the case of E3, where the mean sky level is $\sim 10\ e^-$, Figure 2 of RM04 shows that the CTE correction is typically 0.01 mag. Based on this, we choose not to correct the long-exposure photometry for the CTE effect and proceed to correct the short-exposure photometry using equation (2) of RM04. These corrections are relatively small, amounting to ~ 0.03 mag for the faintest stars on the short-exposure frames, roughly equaling the expected random errors for these stars. To check the efficacy of these corrections, we examine the difference in magnitude of a given star between the long and short exposures as a function of y-position to be sure that there is no trend present. Since the corrections are approximately the same on the F606W and F814W filters, the colors are minimally affected.

We calibrate the photometry to the ACS WFC VEGAmag system, following the procedure given in Bedin et al. (2005) using the most updated encircled energy distributions and the official zero points given by Sirianni et al. (2005). The result of this procedure is photometry that reliably extends from the horizontal branch (HB) to several magnitudes below the main-sequence turnoff (MSTO).[2]

3. COLOR-MAGNITUDE DIAGRAMS

The CMDs derived from our *HST* ACS observations of the target clusters are shown in Figures 1–9. In each case, the plus signs indicate stars affected by at least one saturated pixel in either or both of the F606W and F814W short-exposure images. All four of the metal-poor clusters display predominantly blue HBs along with significant blue straggler sequences. Six of the nine clusters also show rich populations of unresolved main-sequence binaries, as evidenced by the parallel sequences located as much as 0.75 mag brighter than the main sequence. This is not particularly surprising given that we are imaging the central regions of these clusters, where mass segregation has enhanced the binary populations. We should also note that some of these CMDs may contain significant white dwarf sequences. Confirmation of these sequences will require star/galaxy image classification, which will be presented in a future paper.

To fully appreciate the properties of these CMDs, it is important to examine them within the context of existing ground-based photometry of these clusters.

NGC 5466.—The most recent CMDs of this cluster have been presented by Jeon et al. (2004), Rosenberg et al. (2000a), and

[2] Electronic versions of the photometry tables and fiducial sequences are available at http://www.astro.ufl.edu/~ata/GC_Treasury/Web_Page.

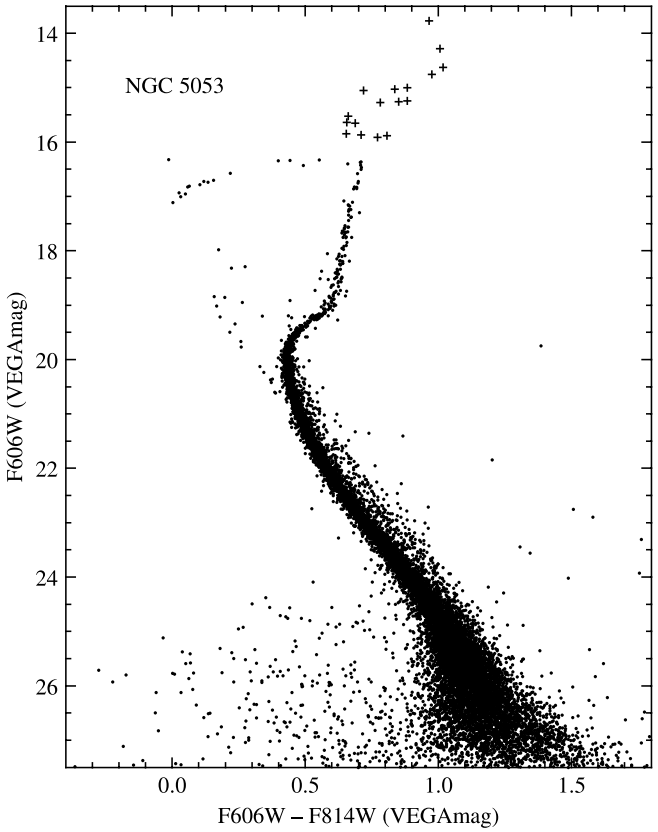

FIG. 3.—Same as Fig. 1, except that the CMD of NGC 5053 is shown, containing 15,618 stars and extending to about 30% of the tidal radius of 14′ (Harris 1996).

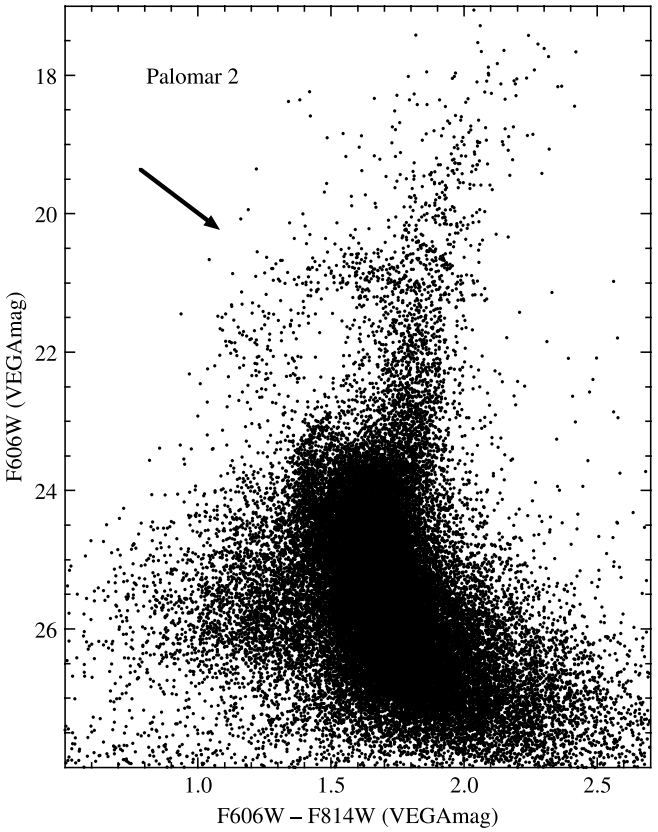

FIG. 5.—Same as Fig. 1, except that the CMD of Palomar 2 is shown, containing 43,242 stars and extending to about 60% of the tidal radius of 6.8′ (Harris 1996). The arrow is the reddening vector for $E(\mathrm{F606W}-\mathrm{F814W}) = 0.3$.

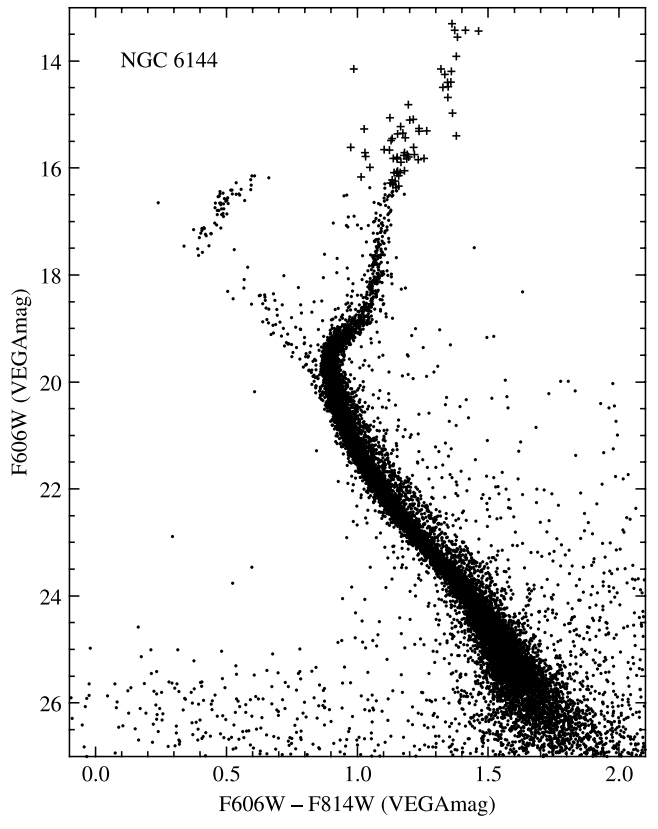

FIG. 4.—Same as Fig. 1, except that the CMD of NGC 6144 is shown, containing 19,442 stars and extending to about 13% of the tidal radius of 33′ (Harris 1996).

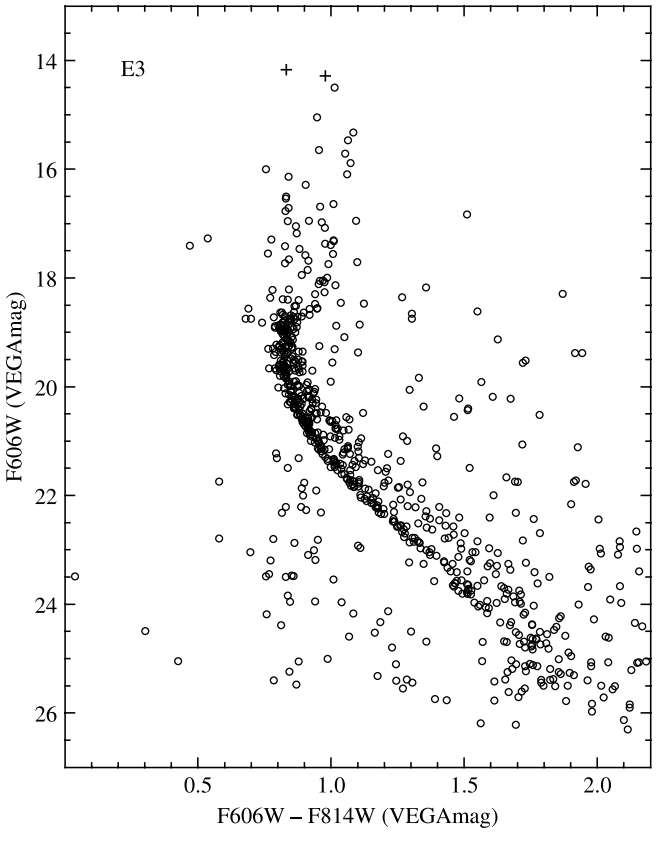

FIG. 6.—Same as Fig. 1. except that the CMD of E3 is shown, containing 852 stars and extending to about 40% of the tidal radius of 11′ (Harris 1996).

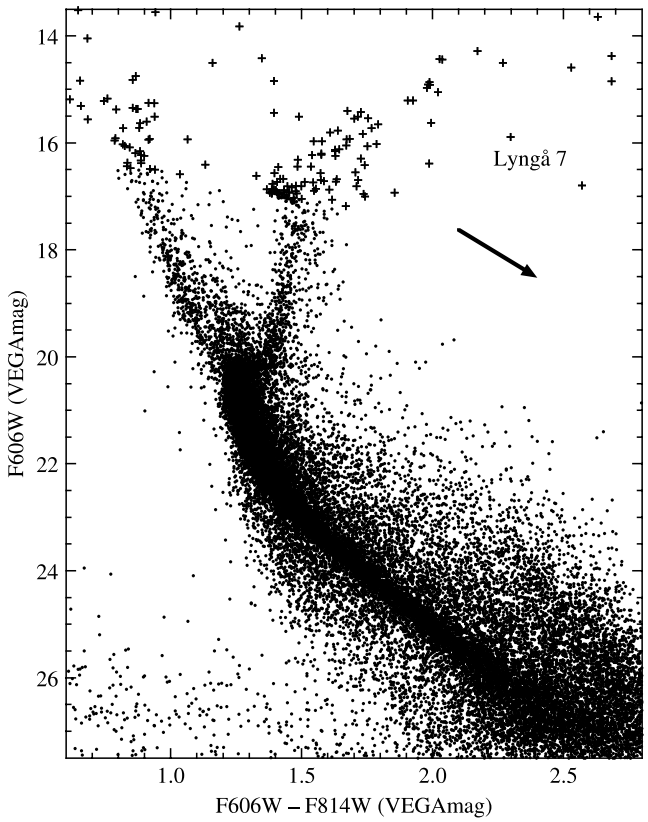

FIG. 7.—Same as Fig. 1, except that the CMD of Lyngå 7 is shown, containing 32,226 stars. The tidal radius for Lyngå 7 is not given in the Harris (1996) compilation. The arrow is the reddening vector for $E(\mathrm{F606W}-\mathrm{F814W})=0.3$.

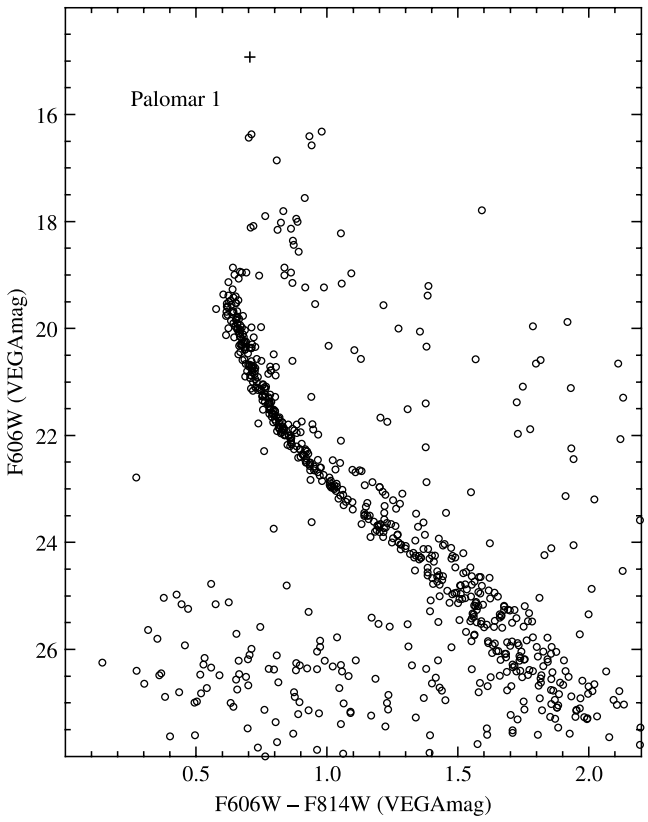

FIG. 8.—Same as Fig. 1, except that the CMD of Palomar 1 is shown, containing 808 stars and extending to about 47% of the tidal radius of 9.0′ (Harris 1996).

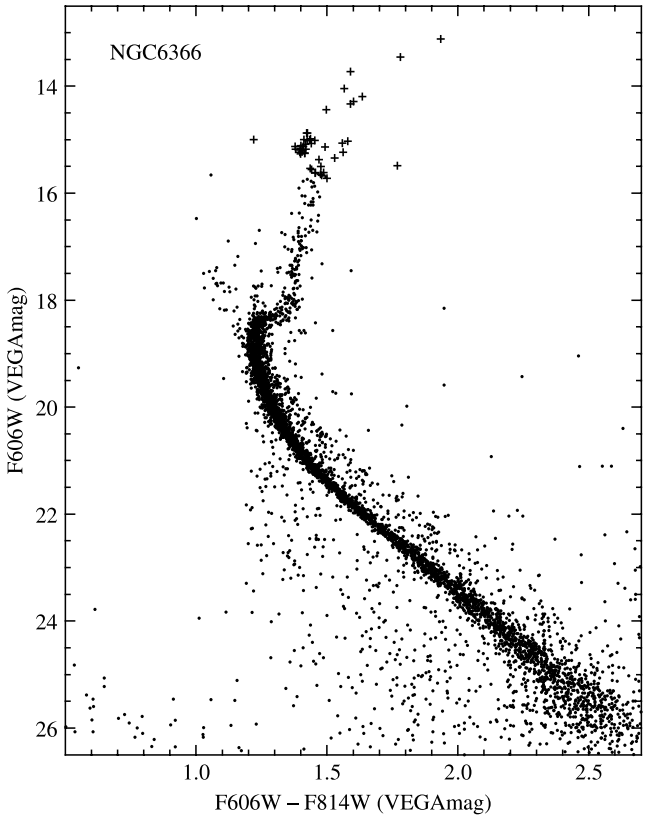

FIG. 9.—Same as Fig. 1, except that the CMD of NGC 6366 is shown, containing 5503 stars and extending to about 27% of the tidal radius of 15′ (Harris 1996).

Corwin et al. (1999). Because of its substantial population of blue stragglers, the majority of prior CMD studies have focused on these stars and their photometric variability. This cluster is of exceptionally low stellar density even near its center; it is probably because of this that NGC 5466 has not been a primary target of *HST* studies. However, it is clear from Figure 1 that our *HST* ACS CMD has revealed the principal sequences of NGC 5466 with significantly higher precision than previous observations.

NGC 6779.—Hatzidimitriou et al. (2004) and Rosenberg et al. (2000a) have both published CCD-based CMDs for this cluster, which reaches past the MSTO. The blue HB and relatively metal-poor nature of the cluster were noted by both studies. In addition, our CMD exhibits a population of blue straggler stars, as well as a better-defined MSTO and unevolved main sequence suitable for age determination.

NGC 5053.—Structurally similar to NGC 5466 discussed above, this cluster also presents an exceptionally low stellar density, which is probably the main reason it has not been previously observed by *HST*. In addition, it also harbors a healthy population of blue straggler stars, making it the focus of numerous stellar brightness variability studies. CMDs have been presented by Rosenberg et al. (2000a), Sarajedini & Milone (1995), and Fahlman et al. (1991), among others.

NGC 6144.—The sole published CMD of this cluster is by Neely et al. (2000); their *BVI* photometry reveals a cluster with a predominantly blue HB and significant differential reddening across its angular extent. This is because NGC 6144 is viewed behind the ρ Ophiuchi dust cloud approximately 40′ northeast of the globular cluster NGC 6121 (M4).

Palomar 2.—Located in a direction of extremely high foreground absorption and differential reddening toward the Galactic anticenter, the CMD of this cluster presented by Harris et al.

TABLE 2
Cluster Parameters

Cluster (1)	$[Fe/H]_{ZW}$ (2)	$[Fe/H]_{CG}$ (3)	$E(B-V)$[a] (4)	$(m-M)_0$[a] (5)	$E(B-V)$[b] (6)	$(m-M)_0$[b] (7)
Target Clusters						
NGC 5466	−2.22	−2.20	0.00	16.00	0.02	16.03
NGC 6779 (M56)	−2.20	−2.00	0.20	15.03	0.26	15.08
NGC 5053	−2.10	−1.98	0.04	16.07	0.01	16.22
NGC 6144	−1.81	−1.56	0.36	14.64	0.45	14.61
Palomar 2	−1.68	−1.42	1.24	17.21	0.94	17.13
E3	−0.80	−0.83	0.30	13.19	0.34	14.54
Lyngå 7	−0.62	−0.64	0.73	14.28	0.78	14.55
Palomar 1	−0.6	−0.7	0.15	15.19	0.23	15.76
NGC 6366	−0.58	−0.73	0.71	12.77	0.75	12.87
Comparison Clusters						
NGC 6341 (M92)	−2.24	−2.16	0.02	14.58	0.025	14.66
NGC 6752	−1.54	−1.24	0.04	13.01	0.035	13.23
NGC 104 (47 Tuc)	−0.71	−0.78	0.04	13.25	0.055	13.40

[a] Data from Harris (1996). Absolute distance modulus has been computed assuming $A_V = 3.1E(B-V)$.
[b] Results from main-sequence fitting.

(1997) exhibits a significant amount of scatter. Nonetheless, these authors were able to characterize the HB morphology of Pal 2 as being bimodal in color, similar to that of NGC 1851, NGC 6229, and NGC 1261. As a result, they suggest that Pal 2 has a metallicity in the range $[Fe/H] \sim -1.3 \pm 0.2$. The features seen by Harris et al. (1997) are also present in Figure 5, with the exception of a second MSTO feature blueward of the dominant main sequence at F606W $\sim$ 23.5 and (F606W − F814W) $\sim$ 1.4. We return to an analysis of this feature and the metallicity of Pal 2 in § 4.2. We note in passing that Pal 2 has gained renewed prominence recently because of a suggestion by Majewski et al. (2004) that it could be associated with the Sagittarius dwarf spheroidal galaxy.

E3.—The first CMD of this cluster was presented by van den Bergh et al. (1980) and later improved on by McClure et al. (1985). Both of these studies noted two intriguing characteristics of this cluster. First, the equal-mass binary sequence in E3 was among the most prominent ever observed to date among GCs. Second, the cluster shows little or no indication of an HB population. Taken together, along with the dramatic decrease in stellar density along the lower main sequence, these findings suggest the presence of significant mass segregation and/or mass loss in E3. Furthermore, these characteristics are consistent with the Galactic GC Pal 13, which Siegel et al. (2001) argue is in the last stages of being destroyed. The fact that E3 does not possess a clear HB makes its distance and age determinations necessarily more uncertain. The most recent CMD by Rosenberg et al. (2000b) corroborates these results.

Lyngå 7.—Thought to be an open cluster originally, Lyngå 7 was studied photometrically by Ortolani et al. (1993), who showed that it is more likely to be a (thick) disk GC. Their CMD is heavily contaminated by noncluster stars, but does reveal a prominent core-helium-burning red clump and a putative main-sequence turnoff that suggests an age significantly younger than other Galactic GCs at its metallicity. However, a reanalysis of the Ortolani et al. (1993) CMD by Sarajedini (2004) indicates an age close to that of 47 Tuc. Our CMD is also heavily contaminated by noncluster stars, but in § 4 we present a radially limited CMD that shows the cluster sequences better.

Palomar 1.—First photometered by Ortolani & Rosino (1985) and later by Borissova & Spassova (1995), Pal 1 is similar to other low-density GCs, such as Pal 13 and E3, in that it exhibits a red giant branch (RGB) and HB that are both very poorly populated. The more recent work of Rosenberg et al. (1998a, 1998b) has revealed a metallicity comparable with that of 47 Tuc, but an age that is some 4–5 Gyr *younger* than 47 Tuc. The possibility that Pal 1 has been misclassified as a GC cannot be ruled out. In fact, Crane et al. (2003) have shown that Pal 1 could be a member of the Monoceros stream, which has open, transitional, and GCs as members (Frinchaboy et al. 2004) and is very interesting considering the ambiguity of Pal 1's classification.

NGC 6366.—From the earliest CMD of this cluster by Pike (1976) to the most recent by Alonso et al. (1997) and Rosenberg et al. (2000a), it has been recognized that NGC 6366 is a close twin of 47 Tuc. Both clusters have predominantly red HBs, a metal abundance close to $[Fe/H] \sim -0.7$, and a sparse RR Lyrae population; and, in fact, NGC 6366 is somewhat closer to us than 47 Tuc. The main reason NGC 6366 has received much less attention than 47 Tuc is because of its high extinction and significant differential reddening.

It is clear from the above discussion that many of the CMD features of these clusters have already been revealed by ground-based observations, especially those at magnitude levels above the MSTO. What makes the *HST* CMDs in Figures 1–9 unique is that they represent the deepest photometry published to date for these clusters. Most extend as much as 7 mag below the MSTO, in some cases revealing a sequence of unresolved binaries that has never before been identified in these clusters. The binary populations of our target clusters will be discussed in a future paper. The *HST* CMDs presented here are ideal for the determination of main-sequence fitting distances, which is the subject of § 4, and ages, which are covered in § 5.

4. MAIN-SEQUENCE FITTING

To minimize systematic errors associated with our filter set, we have chosen to perform main-sequence fitting (MSF) in the ACS F606W and F814W filters. We have selected three "standard"

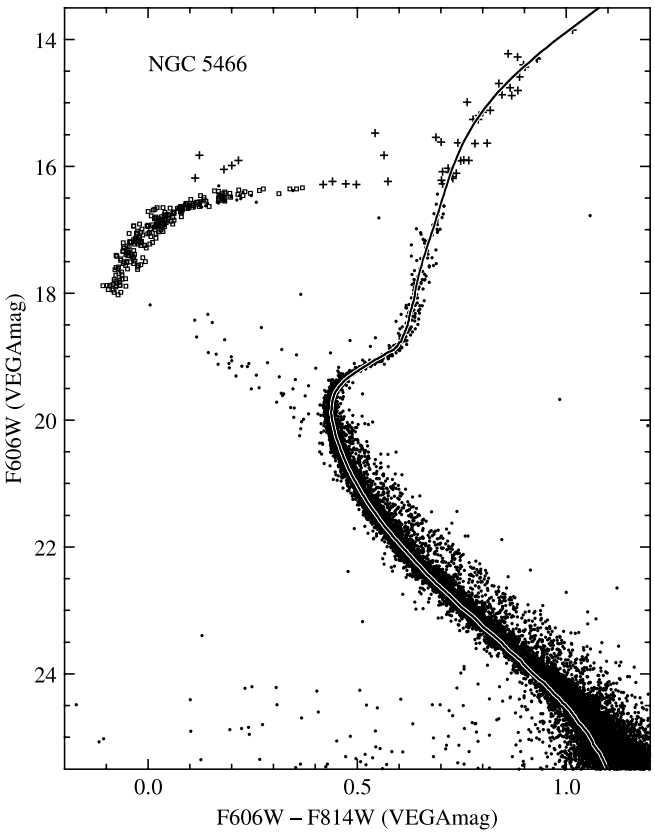

FIG. 10.—Result of fitting the fiducial sequence of M92 to the main sequence of NGC 5466. The squares are M92 HB stars. The plus signs represent stars that are affected by at least one saturated pixel in either or both of the F606W and F814W images.

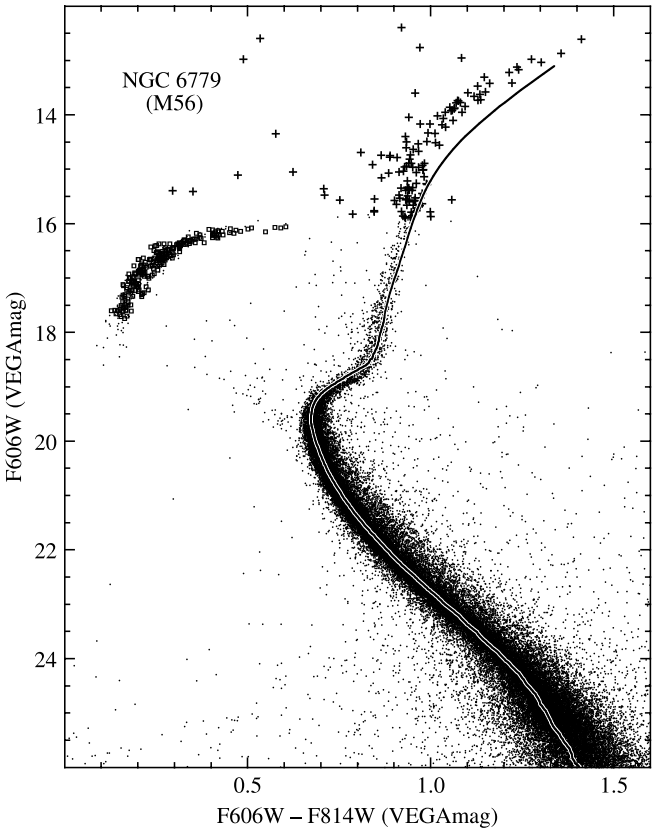

FIG. 11.—Same as Fig. 10, except that the CMD of NGC 6779 (M56) is shown.

clusters from our Treasury database—M92, NGC 6752, and 47 Tuc—as comparison clusters. Our fiducial sequences for M92 and NGC 6752 are consistent with those presented by Brown et al. (2005) and with the ground-based data of Stetson (2000) in the *VI* passbands. However, the Brown et al. (2005) fiducial for 47 Tuc is significantly bluer ($\sim$0.04 mag) than our Treasury data and the photometry of Stetson (2000). We will address these issues more fully in a future paper, but, for the moment, it is important to point out that the MSF performed here makes use of photometry for the target and comparison clusters that is internally consistent.

4.1. *Cluster Properties*

Table 2 lists the properties of the target and comparison clusters in the present study. The metallicities on the Zinn & West (1984) and Carretta & Gratton (1997) scales are taken from a number of sources. For NGC 5466, NGC 5053, NGC 6366, NGC 6752, M92, and 47 Tuc, both $[Fe/H]_{ZW}$ and $[Fe/H]_{CG}$ come from the GC age-dating study of De Angeli et al. (2005), while for Pal 1 these values are measured by Rosenberg et al. (1998a). The Zinn & West (ZW) and Carretta & Gratton (CG) metallicities of NGC 6779 are derived by Hatzidimitriou et al. (2004) as part of their *BVRI* photometric study. For NGC 6144, Lyngå 7, and E3, the ZW values come from Neely et al. (2000), Tavarez & Friel (1995), and Harris (1996), respectively, while the CG metallicities are calculated using the equation in § 2.1 of De Angeli et al. (2005). The metallicity of Pal 2 is derived in § 4.2.

Columns (4) and (5) of Table 2 give the reddening and absolute distance modulus of each cluster from the Harris (1996) catalog. These have generally been calculated assuming $M_v(\mathrm{HB}) = 0.15[\mathrm{Fe/H}] + 0.80$ along with the mean apparent magnitude of

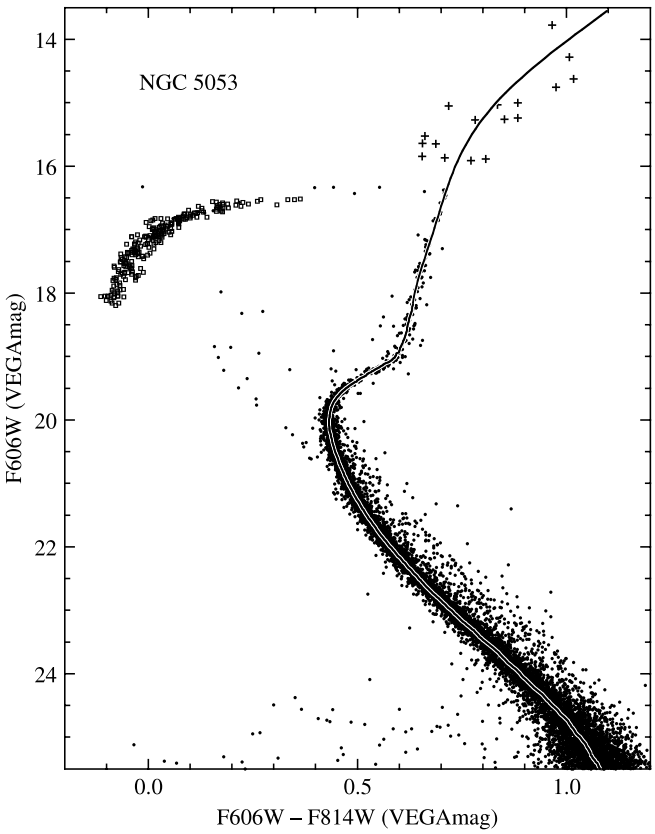

FIG. 12.—Same as Fig. 10, except that the CMD of NGC 5053 is shown.

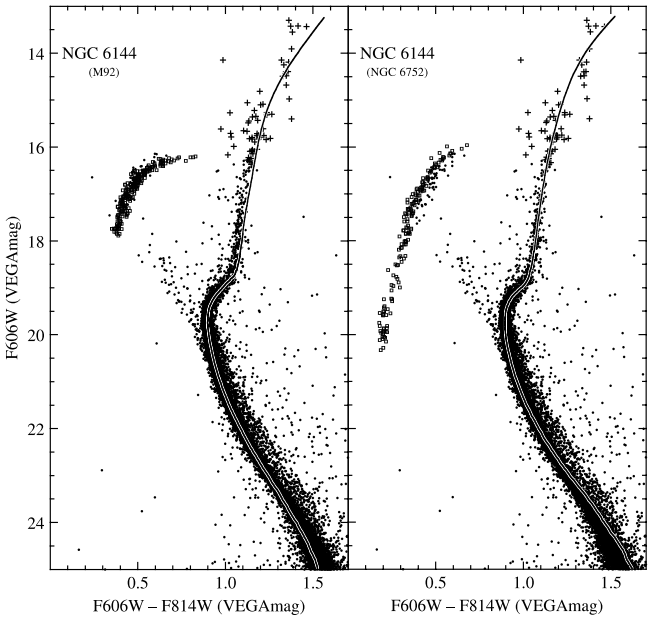

FIG. 13.—Result of fitting the fiducial sequences of M92 (*left*) and NGC 6752 (*right*) to the main sequence of NGC 6144. The squares are the HB stars of M92 (*left*) and NGC 6752 (*right*). The plus signs represent stars that are affected by at least one saturated pixel in either or both of the F606W and F814W images.

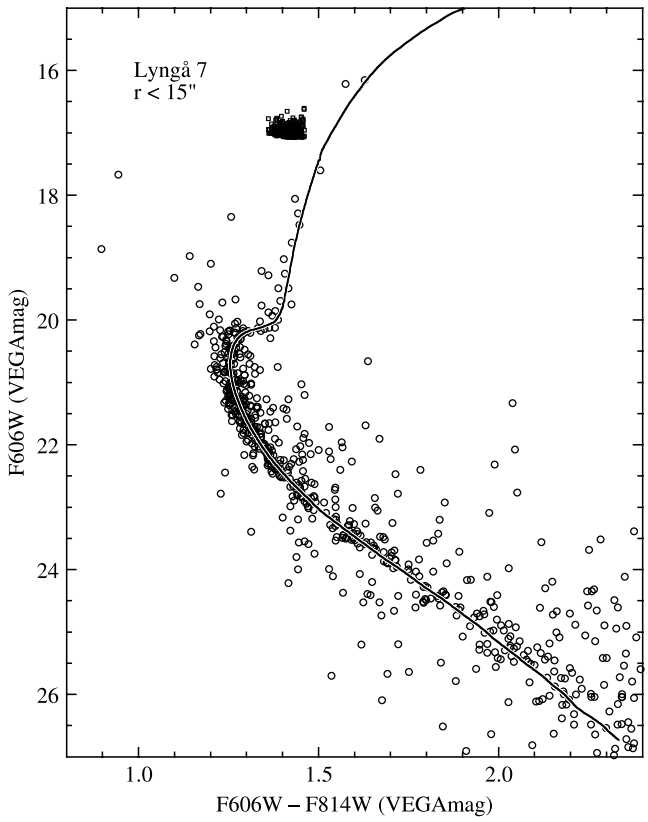

FIG. 15.—Same as Fig. 14, except that the CMD of Lyngå 7 is shown for stars less than 15″ from the cluster center.

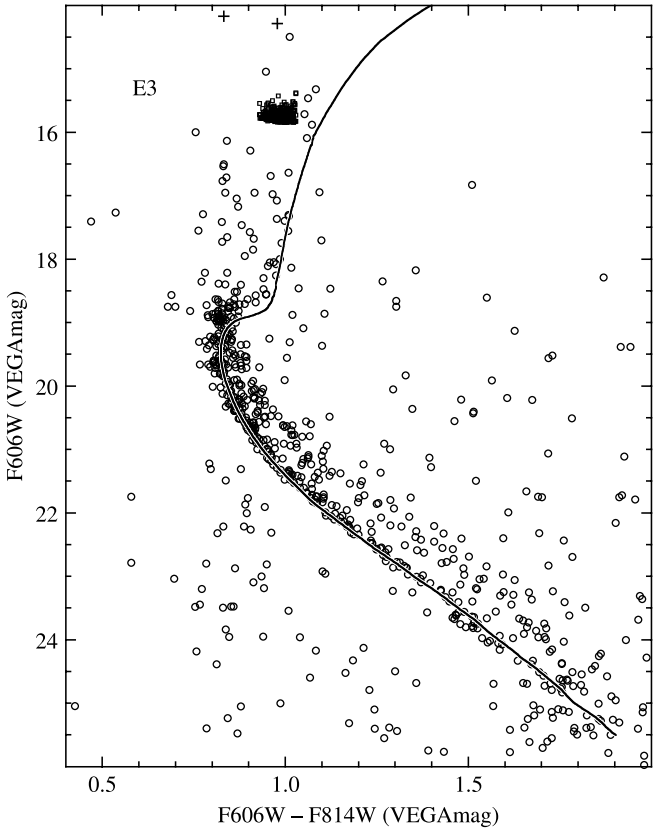

FIG. 14.—Result of fitting our fiducial sequence of 47 Tuc to the main sequence of E3. The squares are the HB stars in 47 Tuc. The plus signs represent stars that are affected by at least one saturated pixel in either or both of the F606W and F814W images.

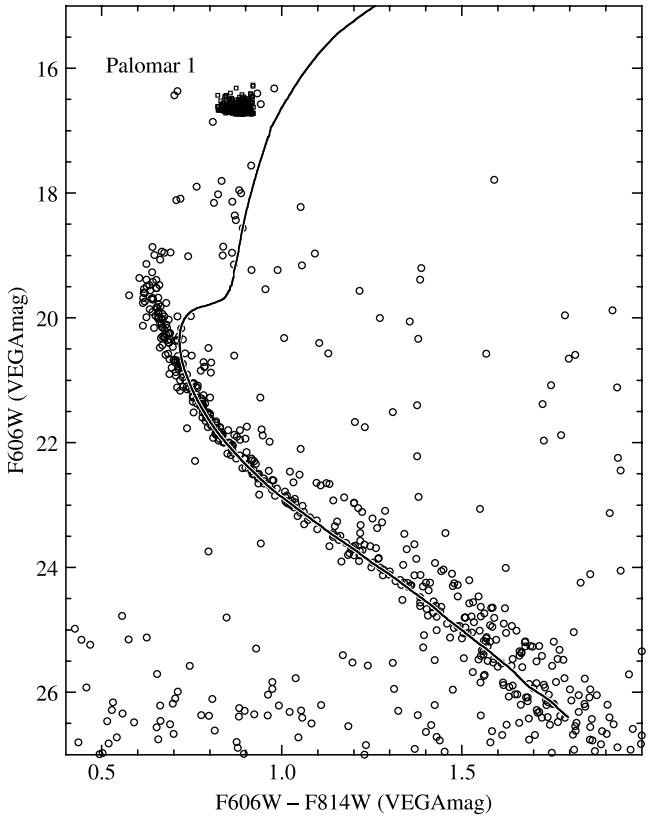

FIG. 16.—Same as Fig. 14, except that the CMD of Pal 1 is shown.

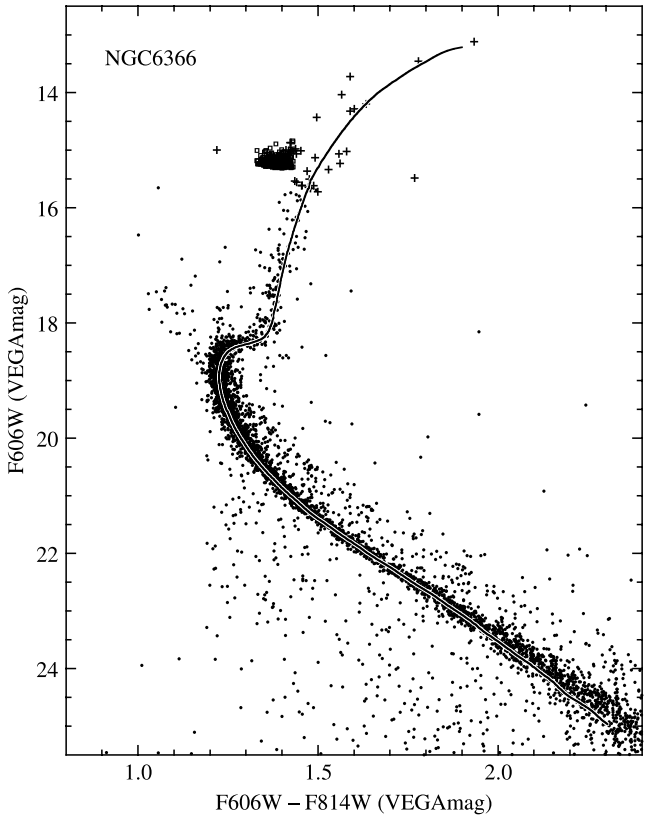

FIG. 17.—Same as Fig. 14, except that the CMD of NGC 6366 is shown.

the HB. This means that in cases where no HB is apparent (e.g., Pal 1, E3) or differential reddening makes the level of the HB difficult to assess (Pal 2), the distances could be highly uncertain. Columns (6) and (7) give the reddenings and distance moduli derived via MSF in this paper. In the case of the comparison clusters, these values are taken from the study of Carretta et al. (2000), in which GC fiducials are fit to local subdwarfs with *Hipparcos* parallaxes.

The main-sequence fits of the comparison cluster fiducials to the cluster CMDs are shown in Figures 10–17. For NGC 6144, because its metal abundance lies between those of two standard clusters (M92 and NGC 6752), we have fit both fiducials to NGC 6144 and interpolated the results. In performing the MS fits, we have shifted the fiducials of the comparison clusters in magnitude and color to match the unevolved main sequence of the target clusters. In particular, we match the data and the fiducial at a point $\sim$2 mag below the MSTO of an old population that occurs at $M_{\mathrm{F606W}} \sim +4.0$. The shifts are then converted to reddenings and distance moduli using the color excess and absorption equations for a G2-type star given by Sirianni et al. (2005), namely $E(\mathrm{F606W} - \mathrm{F814W}) = 0.98E(B - V)$ and $A_{\mathrm{F606W}} = 2.85E(\mathrm{F606W} - \mathrm{F814W})$. The resultant reddenings and distance moduli were derived differentially from those of the comparison clusters. We estimate 1 σ random errors of ± 0.01 and ± 0.05 mag, respectively, in the $E(B - V)$ and $(m - M)_0$ values.

It is instructive to consider our distance modulus results in light of the Harris (1996) values. Excluding E3 and Pal 1, the values in Table 2 reveal a mean difference of $\langle \Delta(m - M)_0 \rangle = 0.07 \pm 0.05$ between our distance moduli and those of Harris (1996) in the sense (Us−Harris). This is not surprising given that the MSF distances of our comparison clusters show a mean difference in

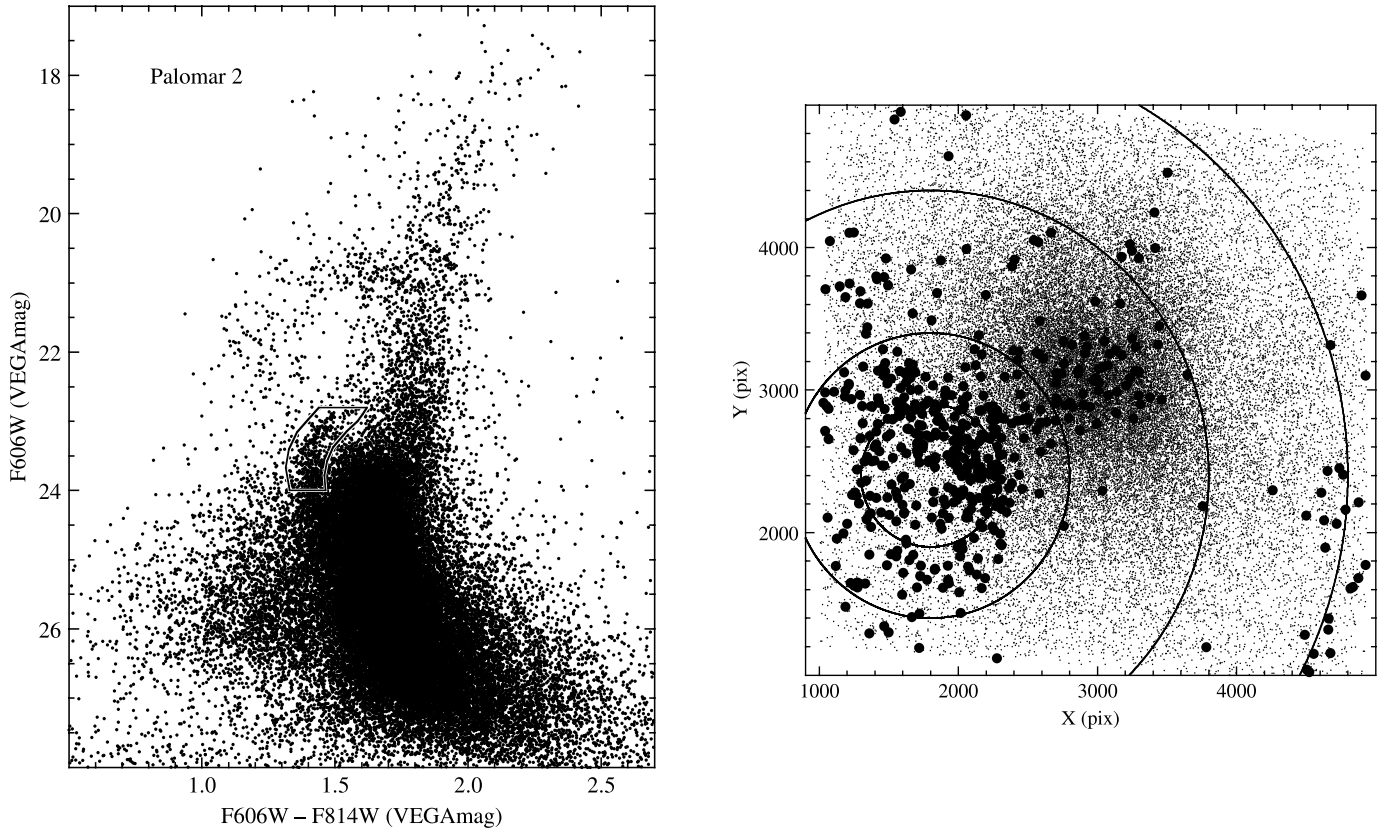

FIG. 18.—*Left*: CMD of Pal 2, with the main-sequence "extension" indicated by a boxlike region. *Right*: Location of stars (*circles*) in this box, relative to other stars in the cluster field. The circles are drawn at radii of 25″, 50″, 100″, and 150″ and centered at (1800, 2400) pixels.

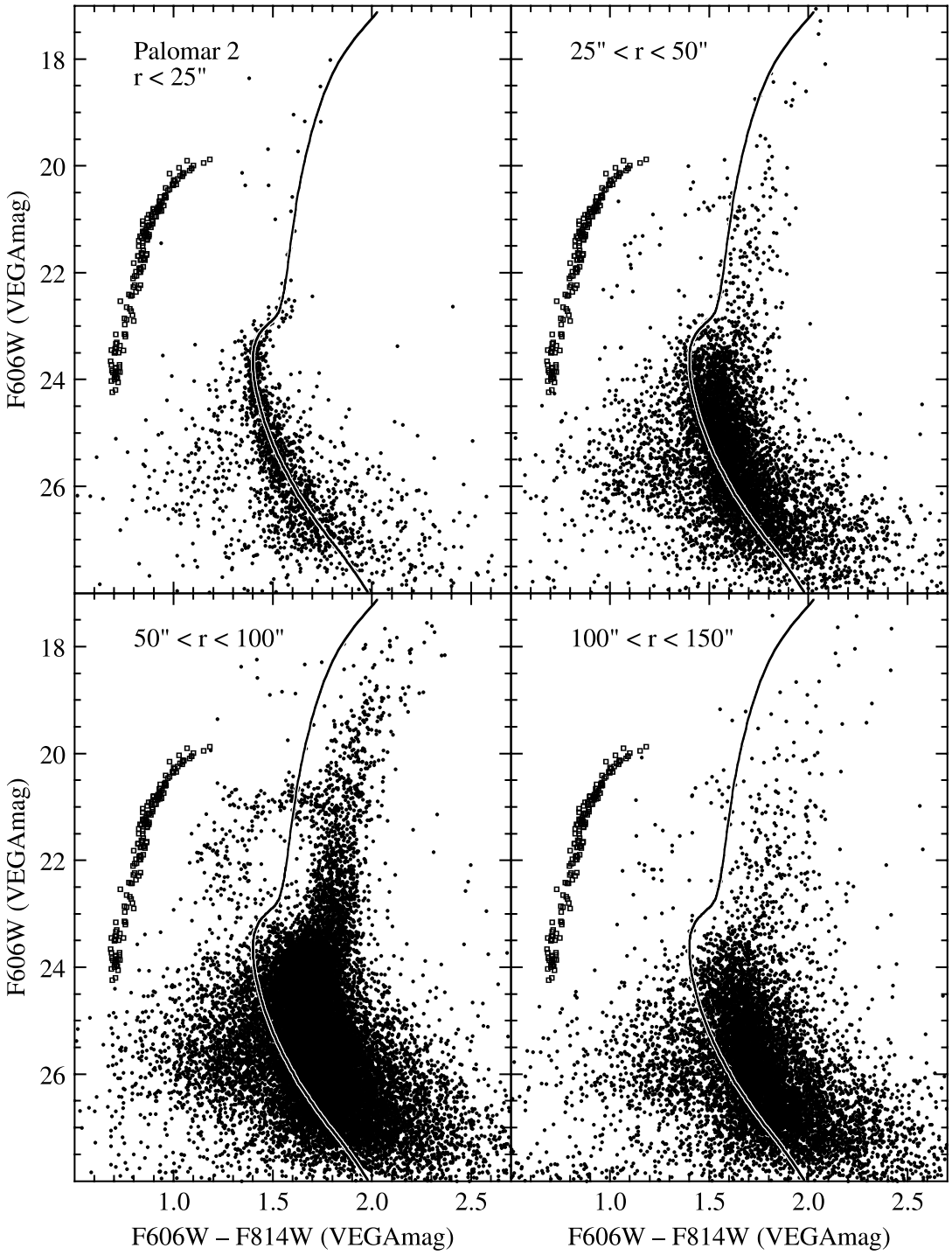

FIG. 19.—Radial CMDs of Pal 2, centered on (1800, 2400) pixels (see Fig. 11). The fiducial and HB stars are those of NGC 6752 shifted to the distance and reddening of the data in the inner region (*top left*).

the same sense of $\langle \Delta(m - M)_0 \rangle = 0.15 \pm 0.02$ relative to the Harris (1996) values. Here and below, we use the small sample statistical formulae of Keeping (1962, p. 202) to calculate the standard error of the mean.

Returning to E3 and Pal 1, neither of these clusters exhibits a significant HB population in its CMD, making the determination of distance especially challenging. The origin of the Harris (1996) distance for E3 is quoted as the McClure et al. (1985) work. However, that paper makes no mention of a distance modulus for E3, so it is not immediately clear what this distance is based on. As a result, it is difficult for us to reconcile the rather large difference of $\Delta(m - M)_0 = 1.35$ mag between our distance modulus and that of Harris (1996) for E3. In the case of Pal 1, the Harris (1996) values are taken from Rosenberg et al. (1998b), who used MSF to 47 Tuc to estimate Pal 1's distance. The precise value of the Pal 1 distance modulus from Rosenberg et al. (1998b) is given as $(m - M)_0 = 15.25 \pm 0.25$; adopting a total error of ± 0.1 mag for our distance modulus determination ($\sigma_{\rm random} \sim 0.05$ mag and $\sigma_{\rm systematic} \sim 0.10$ mag added in quadrature) leads to a difference of $\Delta(m - M)_0 = 0.51 \pm 0.27$ in the sense (Us−Rosenberg), which is not statistically significant.

Turning now to a discussion of our derived reddenings, the mean difference between us and Harris is $\langle \Delta E(B-V) \rangle = 0.044 \pm 0.013$ in the sense (Us−Harris). This excludes Pal 2, which has a very high and uncertain value. In contrast, this difference turns out to be $\langle \Delta E(B-V) \rangle = 0.015 \pm 0.007$ for the comparison clusters. Based on this, one might argue that our derived reddening values are systematically too high. However, a different picture emerges when we compare to the reddening maps of Schlegel et al. (1998). Here we find a mean difference of $\langle \Delta E(B-V) \rangle = -0.010 \pm 0.029$ for the target clusters and $\langle \Delta E(B-V) \rangle = -0.015 \pm 0.014$ for the comparison clusters, suggesting agreement with the Schlegel et al. maps. Note that we have excluded Pal 2 as above from this calculation, and NGC 6144, which is located behind the ρ Ophiuchi dust cloud. We note in passing that the Schlegel et al. (1998) maps yield a reddening of $E(B-V) = 0.91$ for NGC 6144.

In addition to the distances and reddenings that are derived from the MSF procedure, we can also comment on the ages of the target clusters relative to the comparison clusters, which have similar metallicities. In particular, of the nine clusters of interest (the case of Pal 2 is addressed in § 4.2), only Pal 1 appears to be significantly younger than its comparison cluster. There is also some indication that E3 could be younger than 47 Tuc. While earlier work showed that Pal 1 is a relatively young cluster, there is no such expectation for E3, as McClure et al. (1985) actually quoted an age of 18 Gyr for this cluster. However, a more definitive statement about the age of E3 will have to wait for a reliable abundance determination for this cluster. Previous papers on Lyngå 7 (Ortolani et al. 1993; Sarajedini 2004) have suggested that it may be younger than 47 Tuc by as much as ∼4 Gyr. In contrast, our CMD unequivocally shows that the two are about the same age. We return to the subject of cluster ages in § 5. We should note as well that Pal 1 and E3 show a strong depletion of low-mass stars. Even without quantitative luminosity functions, their CMDs show a striking decline of star numbers along the lower main sequence. To fully address this question will require, among other things, a more complete understanding of the photometric completeness of our data. We will address this phenomenon in a future paper.

4.2. *The Special Case of Pal 2*

Of the clusters in this study, Pal 2 is the most problematic in terms of applying the MSF technique. The CMD in Figure 5 presents a main sequence that is so broadened by differential reddening that MSF seems intractable. However, there is an intriguing extension of the main sequence blueward and brightward of the MSTO/SGB (subgiant branch) region, as shown in Figure 18 (*left*). Taking a cue from the photometric study of this cluster by Harris et al. (1997), we hypothesize that this feature represents a minimally reddened population in Pal 2 and proceed to investigate the spatial distribution of these stars. The circles in Figure 18 (*right*) are the stars within the bounded region indicated in the left panel. The appearance of this figure suggests the presence of a region of minimal reddening in the southeast quadrant of the cluster. The concentric circles represent zones approximately centered on this region of Pal 2, for which CMDs are plotted in Figure 19. The exact center of these circles has been chosen to yield a CMD in the innermost zone that best defines the cluster's principal sequences. The line in Figure 19 is the fiducial sequence of NGC 6752 shifted to match the main sequence of Pal 2 inside 25″ from the center. The reddening and distance of Pal 2 listed in Table 2 are derived from these shifts relative to NGC 6752. We estimate an error of ±0.05 in $E(B-V)$ and ±0.10 mag in distance modulus.

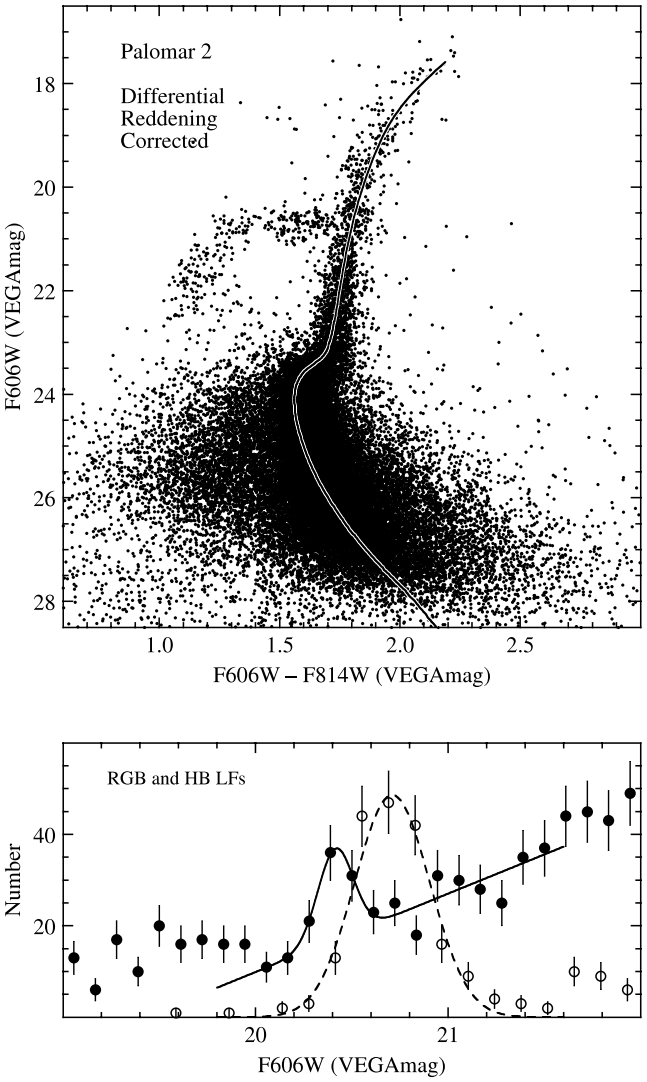

FIG. 20.—*Top*: Differential-reddening-corrected CMD for Pal 2 along with the fiducial sequence of NGC 6752, shifted along the reddening vector to match the principal sequences of Pal 2. *Bottom*: RGB (*filled circles*) and HB (*open circles*) LFs of Pal 2 along with the corresponding Gaussian fits (*solid and dashed lines*).

Figure 19 corroborates our earlier hypothesis that the stars bounded by the region in Figure 18 (*left*) represent a population that is minimally reddened. As we move farther from the southeast quadrant of the cluster, the reddening and its range increase so that the cluster sequences are redder and show greater scatter. In light of this apparent trend in the differential reddening, we have attempted to correct for its effects in the following manner. The first step involves the construction of a fiducial sequence for the cluster. Then each individual star yields a color residual, taken along the reddening direction in the CMD. From these residuals a reddening map is made by finding the median residual in each 256×256 pixel square of the image. Then each star is corrected, along its reddening line, by an amount that is interpolated from the 16×16 points of the reddening map.

The result of this procedure is shown in Figure 20 along with the fiducial sequence of NGC 6752 shifted along the reddening vector to match the principal sequence of Pal 2. The CMD of Pal 2 has tightened up considerably, better defining the HB and the so-called RGB bump that results from a pause in the brightward evolution of RGB stars (Fusi Pecci et al. 1990; Sarajedini & Forrester 1995; Ferraro et al. 1999).

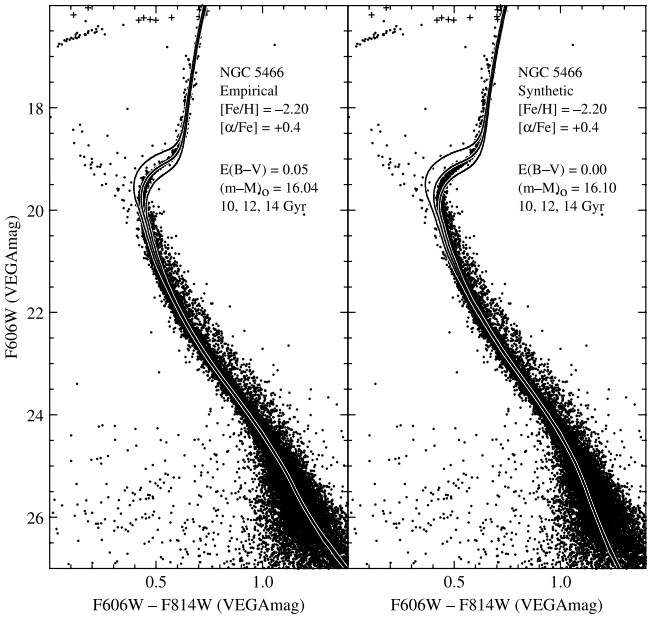

FIG. 21.—CMD of NGC 5466 along with theoretical isochrones based on two different color-$T_{\rm eff}$ transformations (see text).

The luminosity of the RGB bump depends on the cluster metallicity and, to a lesser degree, the cluster age (Alves & Sarajedini 1999). As such, given that Pal 2 is likely to be an old cluster, we can use the magnitude difference between its HB and RGB bump to estimate its metal abundance. Figure 20 (*bottom*) illustrates the luminosity functions (LFs) of the RGB [$1.7 < (\mathrm{F606W} - \mathrm{F814W}) < 2.3$; *filled circles*] and HB [$1.3 < (\mathrm{F606W} - \mathrm{F814W}) < 1.7$; *open circles*], while the solid and dashed lines are the Gaussian fits to these distributions over the range $20.0 < \mathrm{F606W} < 21.6$. These fits yield a difference between the HB and bump magnitudes of $\Delta\mathrm{F606W}_{\rm HB}^{\rm bump} = -0.30 \pm 0.02$. The error has been calculated by adding the standard errors of the mean HB and bump magnitudes in quadrature. Assuming that $\Delta\mathrm{F606W}_{\rm HB}^{\rm bump} \approx \Delta V_{\rm HB}^{\rm bump}$, the relations given in Table 6 of Ferraro et al. (1999) give metallicities of $[\mathrm{Fe/H}]_{\rm ZW} = -1.68 \pm 0.04$ and $[\mathrm{Fe/H}]_{\rm CG} = -1.42 \pm 0.04$. The quoted errors on these quantities represent only the random errors. Thus, the metal abundance of Pal 2 is close to that of NGC 6752. In addition, the close match between the fiducial of NGC 6752 and the Pal 2 CMD suggests that the two clusters have comparable ages and metallicities.

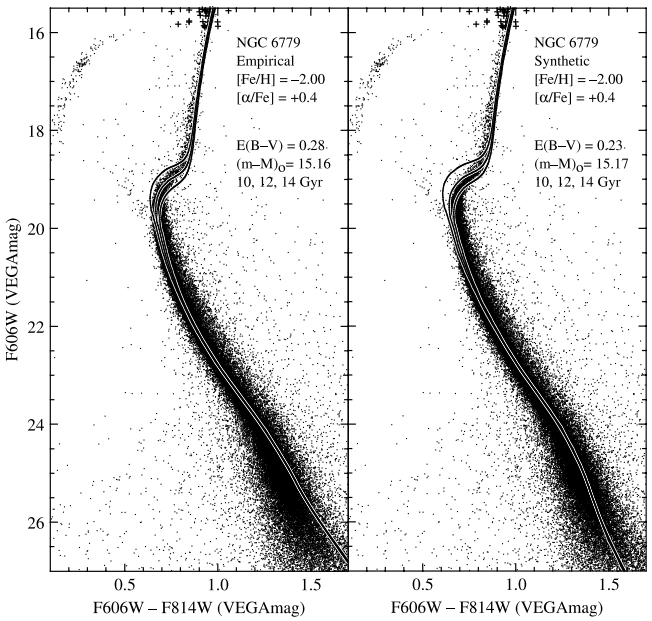

FIG. 22.—Same as Fig. 21, except that the CMD of NGC 6779 (M56) is plotted.

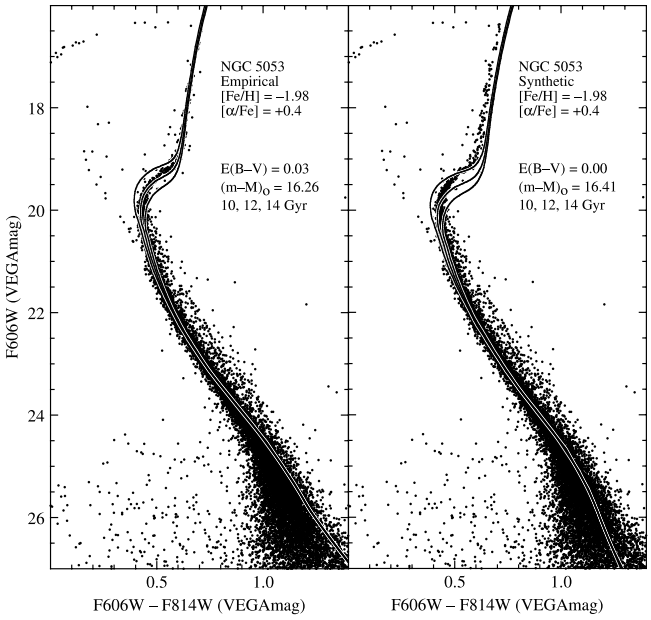

FIG. 23.—Same as Fig. 21, except that the CMD of NGC 5053 is plotted.

5. ISOCHRONE COMPARISONS

5.1. *Construction of Theoretical Isochrones*

Isochrones were generated from stellar evolution tracks produced by the Dartmouth Stellar Evolution Program (DSEP). DSEP employs high-temperature opacities from OPAL (Iglesias & Rogers 1996), low-temperature opacities from Ferguson et al.

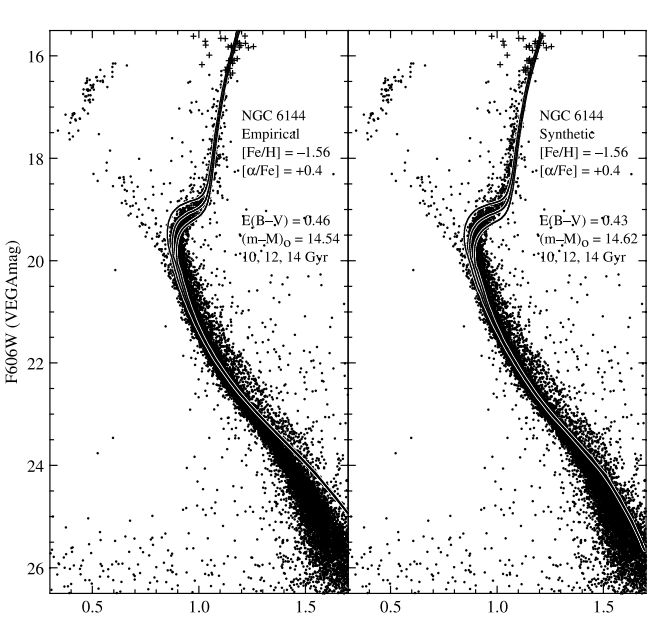

FIG. 24.—Same as Fig. 21, except that the CMD of NGC 6144 is plotted.

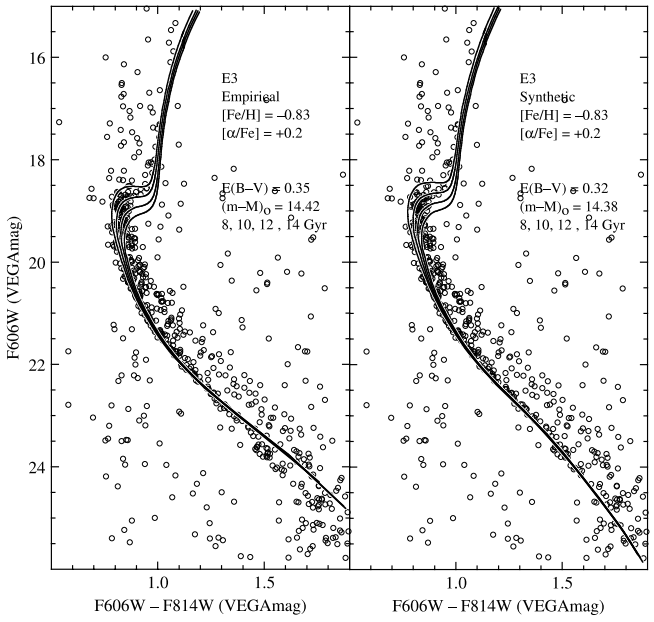

FIG. 25.—Same as Fig. 21, except that the CMD of E3 is plotted.

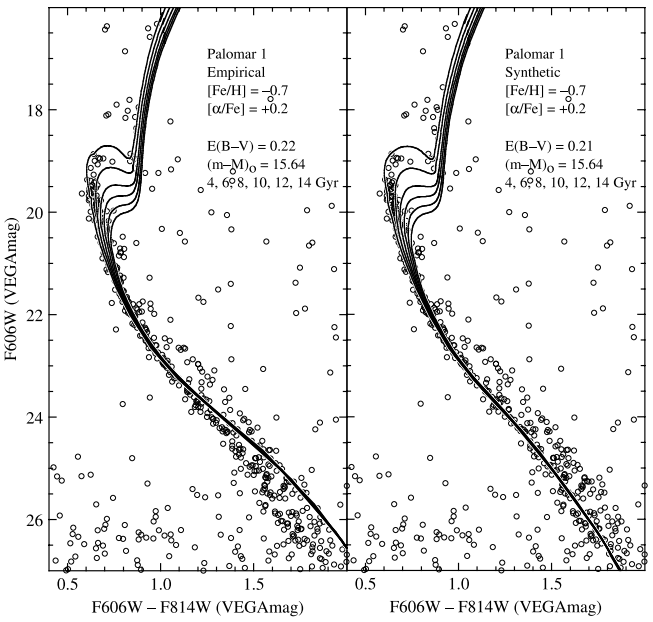

FIG. 27.—Same as Fig. 21, except that the CMD of Palomar 1 is plotted.

(2005), the detailed equation-of-state code FreeEOS[3] for low-mass stars, and surface boundary conditions derived from PHOENIX model atmospheres (Hauschildt et al. 1999a, 1999b). The physical inputs (e.g., opacities, equation of state, and convection theory) used in the stellar interior models are consistent with the physics used in the model atmosphere calculations. A detailed discussion of these new stellar models, color-$T_{\rm eff}$ relations, and isochrones is presented in A. Dotter et al. (2007, in preparation).

A grid of stellar evolution tracks was computed for [Fe/H] = −2.5, −2.0, −1.5, −1.0, −0.5, and 0.0, with $[\alpha/{\rm Fe}] = -0.2$, 0.0, 0.2, 0.4, 0.6, and 0.8. Opacities and surface boundary conditions were created for each specific composition listed. Stellar masses between 0.1 and 1.5 $\mathcal{M}_\odot$ allow for isochrones with ages ranging from 3 to 15 Gyr that extend from $M_V \sim 14$ to the tip of the RGB.

For comparison purposes, the isochrones were transformed using two different color-$T_{\rm eff}$ relations. Both transformations include standard ground-based *B*, *V*, and *I* magnitudes along with the *HST* filters F606W and F814W (both ACS WFC and WFPC2). The semiempirical transformation uses the *B*, *V*, and *I* magnitudes from VandenBerg & Clem (2003) and the relevant equations to convert from *V* and *I* to F606W and F814W in Appendix D of Sirianni et al. (2005). The synthetic color-$T_{\rm eff}$ transformation uses fluxes from the PHOENIX model atmospheres (also used for surface boundary conditions) along with the definitions of *B*, *V*, and *I* from Bessell (1990), and *HST* ACS WFC and WFPC2 filters from Sirianni et al. (2005), all normalized to the Vega system. The semiempirical color transformation

[3] See http://freeeos.sourceforge.net.

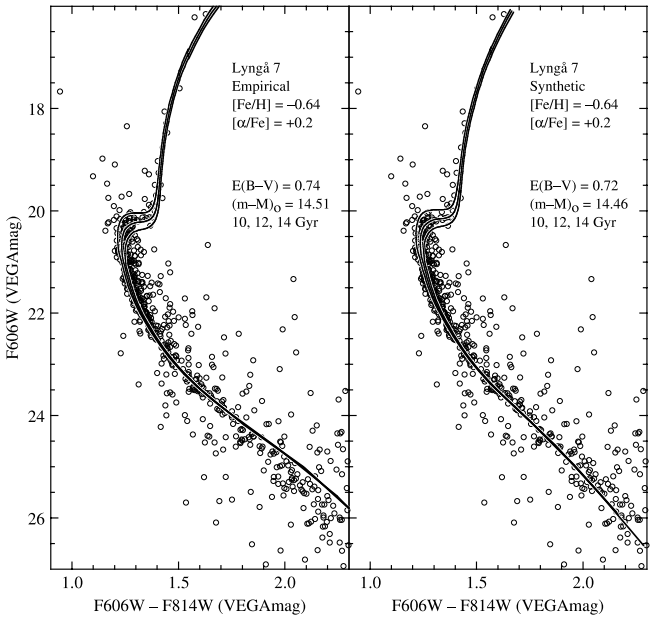

FIG. 26.—Same as Fig. 21, except that the CMD of Lyngå 7 is plotted for stars inside of 15″ from the cluster center.

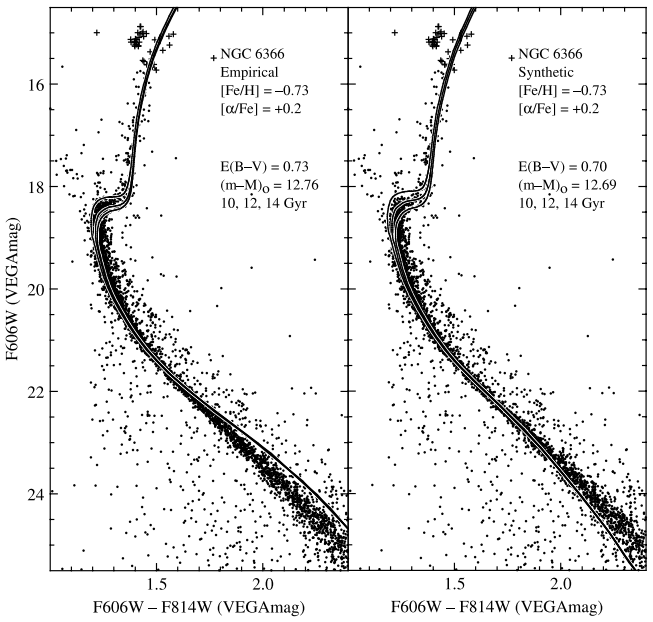

FIG. 28.—Same as Fig. 21, except that the CMD of NGC 6366 is plotted.

has the advantage of being constrained to fit observational data from GCs at low metallicities but does not explicitly account for the effects of α-enhancement. The synthetic color transformation, on the other hand, accounts for the influence of α-enhancement but suffers from poor fits to the MSTO and subgiant regions that are typical of theoretical color transformations.

5.2. *Comparison to Cluster CMDs*

Given that the ZW and CG metallicities usually differ by less than $\sim$0.2 dex, we adopt the latter abundance values for the isochrone fits. To select the appropriate ratio of the α-elements to iron, we assume that $[\alpha/\mathrm{Fe}] = +0.4$ for $[\mathrm{Fe/H}] < -1.0$ and $[\alpha/\mathrm{Fe}] = +0.2$ for $[\mathrm{Fe/H}] \sim -0.7$. These $[\alpha/\mathrm{Fe}]$ values reflect the general trend observed in thick disk and halo stars (e.g., Origlia & Rich 2004; Boesgaard et al. 2005; Meléndez et al. 2006; Reddy et al. 2006). We use the MSF distance and reddening in Table 2 as a starting point; then we vary the distance and reddening until a satisfactory correspondence is achieved between the main sequence of the cluster and the isochrone, making sure that the point $\sim$2 mag below an old MSTO (i.e., $M_{\mathrm{F606W}} \sim +6.0$) matches, similar to the MSF technique performed earlier. The results are shown in Figures 21–28. Pal 2 is excluded because the main sequence is not adequately defined to allow a comparison of the isochrone to the cluster's unevolved main sequence. However, as noted above, its age is likely to be close to that of NGC 6752.

An examination of the isochrone fits reveals the following. The fit to the unevolved main-sequence stars is relatively good for the metal-poor clusters and degrades for the empirical color-T_{eff} transformation as metallicity increases. In this case the models tend to be redder than the observational data. In contrast the synthetic transformation provides a better correspondence with the photometry of the main sequence. The poor match to the lower main sequence could be due to difficulties either with the effective temperatures predicted by the models, or with the color-temperature relations. We are currently investigating this issue.

As expected from the MSF results, the isochrone fits of NGC 5466, NGC 6779, NGC 5053, NGC 6144, Lyngå 7, and NGC 6366 reveal ages in the range of 12–14 Gyr. In contrast, the age of E3 appears to be about 2 Gyr younger than these clusters, while the age of Pal 1 could be as much as 8 Gyr younger. The typical error on these ages is between 1 and 2 Gyr, primarily because they depend on the uncertain distances and reddenings of the clusters. In a future paper, we will address the issues of relative and absolute GC ages using more robust techniques. We emphasize that, as noted in § 4, the age of E3 is likely to be especially uncertain until a more reliable metallicity is determined for it.

6. SUMMARY AND CONCLUSIONS

We have presented the first *HST*-based CMDs for the Galactic globular clusters NGC 5446, NGC 6779, NGC 5053, NGC 6144, Pal 2, E3, Lyngå 7, Pal 1, and NGC 6366. The CMDs extend reliably from the horizontal branch to as much as 7 mag fainter than the main-sequence turnoff. Features revealed in these diagrams include the HB morphology, the presence of blue straggler stars, unresolved binary populations parallel to the main sequence, and possibly white dwarf populations.

Using fiducial sequences for three standard clusters (M92, NGC 6752, and 47 Tuc) with well-known metallicities and distance moduli, we perform main-sequence fitting on the target clusters in order to obtain estimates of their distances and reddenings. These comparisons, along with fitting the cluster main sequences to theoretical isochrones, provide estimates of the clusters' ages. We find that only E3 and Pal 1 are significantly younger than the standard cluster to which they are compared. E3 is $\sim$2 Gyr younger than 47 Tuc, and Pal 1 could be as much as 8 Gyr younger than 47 Tuc. The ages of the remaining clusters are consistent with the standard clusters at their metallicities.

Support for this work (proposal GO-10775) was provided by NASA through a grant from the Space Telescope Science Institute, which is operated by the Association of Universities for Research in Astronomy, Inc., under NASA contract NAS5-26555.

REFERENCES

Alonso, A., Salaris, M., Martinez-Roger, C., Straniero, O., & Arribas, S. 1997, A&A, 323, 374
Alves, D., & Sarajedini, A. 1999, ApJ, 511, 225
Anderson, J. 2006, The 2005 *HST* Calibration Workshop, ed. A. Koekemoer, P. Goufrooij, & L. L. Dressel (Greenbelt: NASA)
Anderson, J., & King, I. 2006, StSCI Inst. Sci. Rep. ACS 2006-01 (Baltimore: STScI), http://www.stsci.edu/hst/acs/documents/isrs/isr0601.pdf
Bedin, L., Cassisi, S., Castelli, F., Piotto, G., Anderson, J., Salaris, M., Momany, Y., & Pietrinferni, A. 2005, MNRAS, 357, 1038
Bessell, M. S. 1990, PASP, 102, 1181
Boesgaard, A. M., King, J. R., Cody, A. M., Stephens, A., & Deliyannis, C. P. 2005, ApJ, 629, 832
Borissova, J., & Spassova, N. 1995, A&AS, 110, 1
Brown, T. M., et al. 2005, AJ, 130, 1693
Carretta, E., & Gratton, R. G. 1997, A&AS, 121, 95
Carretta, E., Gratton, R. G., Clementini, G., & Fusi Pecci, F. 2000, ApJ, 533, 215
Corwin, T. M., Carney, B. W., & Nifong, B. G. 1999, AJ, 118, 2875
Crane, J. D., Majewski, S. R., Rocha-Pinto, H. J., Frinchaboy, P. M., Skrutskie, M. F., & Law, D. R. 2003, ApJ, 594, L119
De Angeli, F., Piotto, G., Cassisi, S., Busso, G., Recio-Blanco, A., Salaris, M., Aparicio, A., & Rosenberg, A. 2005, AJ, 130, 116
Fahlman, G. G., Richer, H. B., & Nemec, J. 1991, ApJ, 380, 124
Ferguson, J. W., Alexander, D. R., Allard, F., Barman, T., Bodnarik, J. G., Hauschildt, P. H., Heffner-Wong, A., & Tamanai, A. 2005, ApJ, 623, 585
Ferraro, F. R., Messineo, M., Fusi Pecci, F., de Palo, M. A., Straniero, O., Chieffi, A., & Limongi, M. 1999, AJ, 118, 1738
Frinchaboy, P. M., Majewski, S. R., Crane, J. D., Reid, I. N., Rocha-Pinto, H. J., Phelps, R. L., Patterson, R. J., & Muñoz, R. R. 2004, ApJ, 602, L21
Fusi Pecci, F., Ferraro, F. R., Crocker, D. A., Rood, R. T., & Buonanno, R. 1990, A&A, 238, 95
Harris, W. E. 1996, AJ, 112, 1487
Harris, W. E., Durrell, P. R., Petitpas, G. R., Webb, T. M., & Woodworth, S. C. 1997, AJ, 114, 1043
Hatzidimitriou, D., Antoniou, V., Papadakis, I., Kaltsa, M., Papadaki, C., Papamastorakis, I., & Croke, B. F. W. 2004, MNRAS, 348, 1157
Hauschildt, P. H., Allard, F., & Baron, E. 1999a, ApJ, 512, 377
Hauschildt, P. H., Allard, F., Ferguson, J., Baron, E., & Alexander, D. 1999b, ApJ, 525, 871
Iglesias, C. A., & Rogers, F. J. 1996, ApJ, 464, 943
Jeon, Y.-B., Lee, M. G., Kim, S.-L., & Lee, H. 2004, AJ, 128, 287
Keeping, E. S. 1962, Introduction to Statistical Inference (Princeton: Van Nostrand)
Majewski, S., et al. 2004, AJ, 128, 245
McClure, R. D., Hesser, J. E., Stetson, P. B., & Stryker, L. L. 1985, PASP, 97, 665
Meléndez, J., Shchukina, N. G., Vasiljeva, I. E., & Ramírez, I. 2006, ApJ, 642, 1082
Neely, R. K., Sarajedini, A., & Martins, D. H. 2000, AJ, 119, 1793
Origlia, L., & Rich, R. M. 2004, AJ, 127, 3422
Ortolani, S., Bica, E., & Barbuy, B. 1993, A&A, 273, 415
Ortolani, S., & Rosino, L. 1985, Mem. Soc. Astron. Italiana, 56, 105
Pike, C. D. 1976, MNRAS, 177, 257
Reddy, B. E., Lambert, D. L., & Allende Prieto, C. 2006, MNRAS, 367, 1329
Reiss, A., & Mack, J. 2004, STScI Inst. Sci. Rep. ACS 2004-006 (Baltimore: STScI), http://www.stsci.edu/hst/acs/documents/isrs/isr0406.pdf (RM04)
Rosenberg, A., Aparicio, A., Saviane, I., & Piotto, G. 2000a, A&AS, 145, 451
Rosenberg, A., Piotto, G., Saviane, I., & Aparicio, A. 2000b, A&AS, 144, 5

Rosenberg, A., Piotto, G., Saviane, I., Aparicio, A., & Gratton, R. 1998a, AJ, 115, 658
Rosenberg, A., Saviane, I., Piotto, G., Aparicio, A., & Zaggia, S. R. 1998b, AJ, 115, 648
Sarajedini, A. 2004, AJ, 128, 1228
Sarajedini, A., & Forrester, W. 1995, AJ, 109, 1112
Sarajedini, A., & Milone, A. A. E. 1995, AJ, 109, 269
Schlegel, D. J., Finkbeiner, D. P., & Davis, M. 1998, ApJ, 500, 525
Siegel, M. H., Majewski, S. R., Cudworth, K. M., & Takamiya, M. 2001, AJ, 121, 935
Sirianni, M., et al. 2005, PASP, 117, 1049
Stetson, P. B. 2000, PASP, 112, 925
Tavarez, M., & Friel, E. 1995, AJ, 110, 223
VandenBerg, D. A., & Clem, J. L. 2003, AJ, 126, 778
van den Bergh, S., Demers, S., & Kunkel, W. E. 1980, ApJ, 239, 112
Zinn, R. J., & West, M. J. 1984, ApJS, 55, 45

Note added in proof.—We have been experimenting with deriving reliable magnitudes for the saturated stars on our images using the algorithm of R. L. Gilliland (ACS CCD Gains, Full Well Depths, and Linearity up to and beyond Saturation [ISR ACS 2004-01; Baltimore: STScI; 2004]). Our results suggest that we can significantly improve the photometry of the brightest stars using these techniques. As a result, our final pass photometry will include magnitudes measured in this manner for the saturated stellar profiles. This will extend the dynamic range of our CMDs from the lower main sequence to near the tip of the red giant branch.